Petal-like CdS nanostructures coated with exfoliated sulfur-doped carbon nitride via chemically activated chain termination for enhanced visible-light–driven photocatalytic water purification and H₂ generation

Yan Wu[a], Hou Wang[a,b,**], Wenguang Tu[a], Shuyang Wu[a], Yue Liu[a], Yong Zen Tan[a,c], Hanjin Luo[d], Xingzhong Yuan[b], Jia Wei Chew[a,c,*]

[a] School of Chemical and Biomedical Engineering, Nanyang Technological University, Singapore, 637459, Singapore
[b] College of Environmental Science and Engineering, Hunan University, Changsha, 410082, China
[c] Singapore Membrane Technology Center, Nanyang Environment and Water Research Institute, Nanyang Technological University, Singapore, 639798, Singapore
[d] College of Environment and Energy, South China University of Technology, Guangzhou, 510006, China

A B S T R A C T

Novel composite photocatalysts consisting of petal-like cadmium sulphide (CdS) nanoparticles and varying amounts of exfoliated sulfur-doped carbon nitride (SCN) were successfully prepared. The as-obtained materials were characterized by field emission scanning electron microscopy, X-ray diffraction, X-ray photoelectron spectroscopy, ultraviolet–visible diffuse reflection spectroscopy, photoluminescence spectroscopy and photo-current-time measurement. Results indicate a strong electric coupling interaction between SCN and CdS due to the heterojunction formed at the amine functionalities sites and oxidized chain terminations of SCN. Two typical pollutants like rhodamine B (RhB) and colorless bisphenol A (BPA) were used for the evaluation of photo-catalytic activity. The best-performing CdS/SCN composite (i.e., CS5) synthesized exhibited enhanced visible-light-driven photocatalytic RhB efficiency of about 8.71 and 4.06 times higher than those of pure exfoliated SCN and CdS, respectively. As for BPA degradation, the CS5 composite was 9.00 and 3.61 times more efficient than that of exfoliated SCN and CdS, respectively. These excellent performances were found to be attributable to the remarkable charge carrier separation between CdS and exfoliated SCN with the aid of heterojunction interfacial structures. More importantly, the exfoliated SCN substantially reinforced the photostability of the CdS nano-particles. Evaluation of the photocatalytic H₂ evolution showed that the visible-light H₂ production rate of the best-performing CS5 composite was also much greater than the constituents at 247.72 μmol h⁻¹ g⁻¹. Cyclic tests demonstrated the stability of the CS5 composite over repeated use. A possible mechanism was proposed to explain the photocatalytic reaction process. This study provides new insights into the preparation of highly efficient and stable sulfide-based composite photocatalysts, which are promising for implementation in wide-ranging environmental applications.

1. Introduction

Photocatalysis is well acknowledged as an effective method for the abatement of aqueous pollutants in wastewater treatment and environmental remediation. Various semiconductor photocatalysts have been employed in this regard in the last few years [1–3]. In particular, graphitic carbon nitride (g-C₃N₄) materials have received substantial interest in the academic community as a novel generation of photo-catalysts because of their facile synthesis procedures and apt electronic band structures with narrow band gaps of about 2.7 eV [4]. In addition,

g-C₃N₄ possesses high physicochemical stability due to its π-π con-jugated framework which connects the two-dimensional layered structure of tri-s-triazine building blocks [5]. These unique properties make g-C₃N₄ a promising metal-free semiconductor photocatalyst in several applications such as solar energy conversion and wastewater treatment [6,7].

Unfortunately, the pure g-C₃N₄ has limited photocatalytic efficiency because of low quantum efficiency and high recombination rate of photogenerated electron–hole pairs [8,9]. To overcome these problems, numerous strategies have been devised to enhance the efficiency of

---

pristine g-C$_3$N$_4$, such as doping with either non-metal [10] or metal [11] elements, and forming composites with other chemical compounds [12,13]. Regarding doping, Liu et al. prepared sulfur-doped g-C$_3$N$_4$ by treating the g-C$_3$N$_4$ powder at 450 °C in high-purity gaseous H$_2$S atmosphere [14]. However, this method would produce much poisonous and foul-odor gas, which can be overcome by synthesizing sulfur-doped g-C$_3$N$_4$ by heating thiourea as a starting material, as done in this study. The other promising strategy is to couple carbon nitride materials with other semiconductors to enhance the photocatalytic activity of bare g-C$_3$N$_4$. In theory, due to the combination of g-C$_3$N$_4$ with another semiconductor that has well-matched valence band and conduction band edge potentials, heterojunctions are formed between the two components, which improve efficient separation of the photogenerated electrons and holes in the interfacial contact [15,16]. Among various semiconductors reported, CdS, as one of the narrow bandgap semiconductors (2.2–2.4 eV), has applications in a wide range of fields including optoelectronics [17], photovoltaics [18], chemical sensors [19] and photocatalysis [20–22]. It has been extensively investigated as a visible-light-driven photocatalyst and its photocatalytic activity has been found to be affected by a variety of factors including preparation conditions, particle size, morphology, and crystallinity [23]. However, there is an inherent drawback for CdS-based photocatalysts, namely, the photocorrosion problem [24,25] in which the sulfide ion is highly prone to oxidation by photogenerated holes. The photocorrosion effect makes CdS unstable as a photocatalyst thereby greatly obstructs its practical application. It is therefore absolutely vital to develop suitable surface engineering methods to inhibit photocorrosive damage to the CdS nanoparticles. Towards this end, coating CdS with the exfoliated sulfur-doped carbon nitride (SCN) may be an effective method to stabilize the surface and inhibit the photocorrosion process [26]. As revealed by optical spectroscopic measurements, the exfoliated SCN not only significantly reduced the amount of surface traps, but also provided chemical protection to inner CdS nanoparticles. As a result of the exfoliated SCN protection, the photocorrosion of CdS was successfully inhibited.

On the basis of the above concepts, synergy could be obtained by combining the two strategies to enhance photocatalytic activity of g-C$_3$N$_4$ of non-metal element doping and hybridization with another semiconductor. Accordingly, the one-pot fabrication of CdS/SCN photocatalysts with different exfoliated SCN content was the target of this work. The hybrid samples were rigorously characterized and then the corresponding photocatalytic activities were examined for the photodegradation of Rhodamine B (RhB) and bisphenol A (BPA) under visible light irradiation. The photodegradation activity of the composites with varying exfoliated SCN content was investigated vis-à-vis the bare exfoliated SCN and CdS, and the underlying mechanisms were explored by using photoluminescence spectroscopy, photocurrent-time measurement, the active species trapping experiments and electron spin resonance (ESR) analysis. The results here are expected to be valuable for potential applications in the water purification field, and in the efficient utilization and conversion of solar energy.

2. Experiment

2.1. Material synthesis

All reagents were of analytical grade from Sigma-Aldrich, and used as received without further purification. Double deionized water was used for the synthesis.

2.1.1. Synthesis of bulk sulfide-doped carbon nitride (SCN)

The bulk SCN sample was prepared as the previous method [27]. In brief, 10 g thiourea was placed in a alumina crucible and heated in air atmosphere at 550 °C for 5 h at the heating rate of 3 °C/min, then left to naturally cool to room temperature before being ground with a mortar and pestle prior to characterization.

2.1.2. Synthesis of pristine sulfide-doped carbon nitride (SCN) nanosheet

The SCN nanosheet was obtained via thermal oxidation exfoliation of initial bulk SCN in air [28]. In short, 2 g of bulk SCN was exposed to air and calcined at 550 °C for 5 h, and the powder obtained was collected for use as a reference.

2.1.3. Synthesis of exfoliated SCN

80 mg SCN nanosheet was carefully added to a mixture of 30 mL of concentrated nitric acid (70%) and 10 mL of concentrated sulfuric acid (98%). The solution was sonicated (Elmasonic S 50R) for 1 h and magnetically stirred for 23 h in a fume hood. The homogeneous solution was added to 200 mL of deionized (DI) water, centrifuged and washed with deionized water to obtain a neutral pH. The resultant powder was dried and ground with a mortar and pestle.

2.1.4. Synthesis of exfoliated SCN coated CdS particles (CdS/SCN)

In a typical synthesis, CdCl$_2$·2.5H$_2$O (4 mmol), thiourea (TU; 4 mmol), and polyvinylpyrrolidone (PVP; 0.45 g) were dissolved in 40 mL of deionized (DI) water using sonication. Then the targeted amount of exfoliated SCN was added and sonication continued for 1 h followed by 6 h of magnetic stirring. Specifically, the mass of exfoliated SCN added was either 20, 50, 80 or 100 mg during the synthesis process, and the resulting hybrids were denoted as CS2, CS5, CS8 and CS10, respectively. The homogeneous mixture obtained was transferred into a Teflon-lined stainless-steel autoclave (50 mL) and kept at 160 °C for 12 h in an electric oven. After cooling to room temperature naturally, the products were collected by centrifugation, washed with anhydrous ethanol and distilled water several times, and finally dried in air at 80 °C for 10 h. The synthesis procedure for CdS particles is the same as that for CdS/SCN synthesis but without the addition of exfoliated SCN into the starting reaction mixture. The overall procedure of the preparation of the CdS/SCN photocatalyst is depicted in Fig. 1.

2.2. Characterization methods

Transmission electron microscope (TEM) images were obtained using the JEOL 2010 HR & UHR (Japan) operated at an accelerating voltage of 100 kV. The freshly prepared sample was dispersed by ultrasound before characterization. Scanning electron microscope (SEM) images were obtained using the JEOL JSM 6700F (Japan) in different magnifications at an accelerating voltage of 15 kV. UV–visible diffuse-reflectance spectra (UV–vis DRS) were recorded in the range of 200–800 nm with a UV-2450 spectrometer equipped with an integrating sphere. The powder X-ray diffraction (XRD) patterns were recorded using Bruker AXS D8 Advance diffractometer operating with the Cu-Ka source to investigate the crystal structure of the samples. The X-ray photoelectron spectroscopy (XPS) measurements were conducted with an Axis Ultra DLD spectrometer (Kratos Analytical Ltd., England) with amonochromatized Al Ka X-ray source (hm = 1486.6 eV). Photoluminescence (PL) spectroscopy was measured at the excitation wavelength of 300 nm at room temperature by Perkin-Elmer LS-55 spectrofluorimeter. The time-resolved fluorescence decay spectrum was performed on an Edinburgh FLS980 spectrophotometer at an excitation wavelength of 300 nm. The electron spin resonance (ESR) signals of radicals spin-trapped by spin-trapped reagent 5, 5-dimethyl-*l*-pyrroline *N*-oxide (DMPO) and 2,2,6,6-Tetramethylpiperidinooxy (TEMPO) were examined via a Bruker ER200-SRC spectrometer under visible light irradiation (λ > 420 nm). Photocurrent-time (PT) was tested with a CHI 660C electrochemical station in a standard three-electrode configuration.

2.3. Photocatalytic activity test

2.3.1. Evaluation of RhB solution and BPA solution

The photocatalytic activity of the CdS/SCN (CS) composite was evaluated by the extent of degradation of Rhodamine B (RhB) and

Fig. 1. Schematic representation of formation mechanism of exfoliated sulfur-doped carbon nitride (SCN) and CdS/SCN composite.

bisphenol A (BPA) under visible light irradiation. A 300 W Xenon lamp with an UV cut-off filter ($\lambda > 420$ nm) was used as a visible light source (20 V, 15 A, 15 cm away from the photocatalytic reactor). For the decomposition of RhB or BPA, 50 mg of the CS photocatalyst was dispersed in 100 mL of 10 mg/L RhB or BPA aqueous solution. The solution was continuously magnetically stirred with a magnetic bar during irradiation to ensure homogeneity. Prior to the photoreaction, the suspension was magnetically stirred in the dark for 60 min to attain adsorption/desorption equilibrium. Upon irradiation, 3 mL samples were withdrawn from the suspension every 15 min for up to 90 min. After that, the CS composite particles were removed via centrifugation (10000 rpm for 10 min). The RhB concentration in the samples were quantified with a UV–vis spectrophotometer at the wavelength of 554 nm (UV-2450, Shimadzu, Japan), while the concentration of BPA were analyzed by high performance liquid chromatography (HPLC; Shimadzu LC-20AT, Tokyo, Japan) whereby the mobile phase was a mixture of methanol and water (V/V = 70/30) fed at a flow rate of 1 mL/min and the injection volume was set as 20 μL.

2.3.2. Evaluation of H₂ evolution

The evolution of H_2 released is also an indicator of photocatalytic activity. 50 mg of the catalyst was dispersed in 100 mL aqueous solution of lactic acid (10 vol%) under magnetic stirring. A 250 mL top-irradiation quartz reaction vessel was connected to an enclosed vitreous gas recirculation system, and a 300 W Xe lamp was used as the light source, with a cut-off filter was applied to generate visible light ($\lambda > 420$ nm). Prior to the photoreaction, the system was vacuumed to completely remove air and the dissolved oxygen. The reaction temperature was maintained at room temperature through the cooling water circulation system and the accumulated amount of evolved gases was monitored in situ every 60 min interval using a gas chromatograph equipped with a thermal conductive detector (TCD).

3. Results and discussion

3.1. Structure and morphology

The crystal structure and phase composition of the synthesized samples were investigated by using XRD, and the representative XRD patterns of exfoliated SCN, CdS and CS composites are shown in Fig. 2. For pure exfoliated SCN, the strong diffraction peak at 27.6° reflects the characteristic interlayer-stacking of the conjugated aromatic system
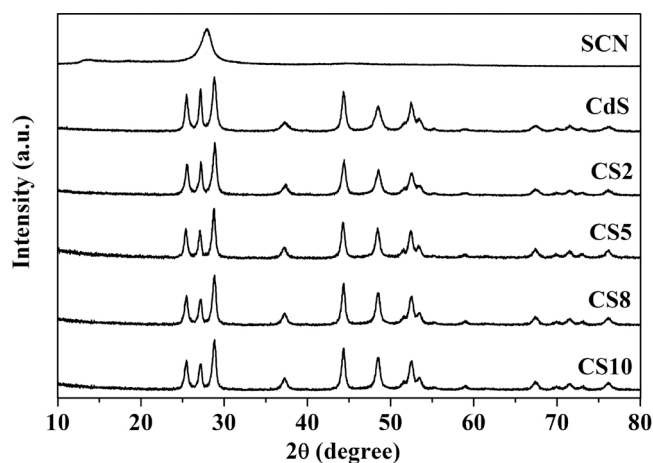

Fig. 2. XRD patterns of exfoliated SCN, CdS and CS composites with varying amounts of exfoliated SCN.

with a *d* spacing of 0.326 nm, which is representative of graphitic materials, while the minor diffraction peak at 13.1° represents the in-plane structural packing motif corresponding to a *d* spacing of 0.672 nm [29–31]. The pure CdS sample displays major diffraction peaks at 2θ of 25.3°, 26.9°, 28.7°, 37.1°, 44.3°, 48.4°, and 52.5° corresponding to the crystalline planes of (100), (002), (101), (102), (110), (103) and (201), respectively, which can be indexed to the hexagonal phase of CdS with lattice constants of a = 4.140 Å and c = 6.719 Å (JCPDS: 41-1049) [32]. As for the CS composites, the XRD patterns exhibit characteristic diffraction peaks of hexagonal CdS phases, and the peak intensities changed as the exfoliated SCN content in the composite increased, although the peak corresponding to the exfoliated SCN can hardly be discerned due to the lower composition. Nonetheless, the presence of exfoliated SCN in the CS composites can be evidenced by SEM and XPS analyses, as discussed later.

The morphological structures of the as-prepared photocatalysts were investigated by SEM and TEM. Fig. 3(a–d) shows the SEM images of the exfoliated SCN, CdS and CS5 composite. The as-synthesized exfoliated SCN in Fig. 3(a) has approximately uniform sizes of < 50 nm, while the CdS nanoparticles in Fig. 3(b) has sizes between 200–300 nm and each was made up of four petal-like sub-units. Specifically, each petal had a cone-like shape, and the assembly of four petals into this kind of geometry provided a large surface area of these anisotropic
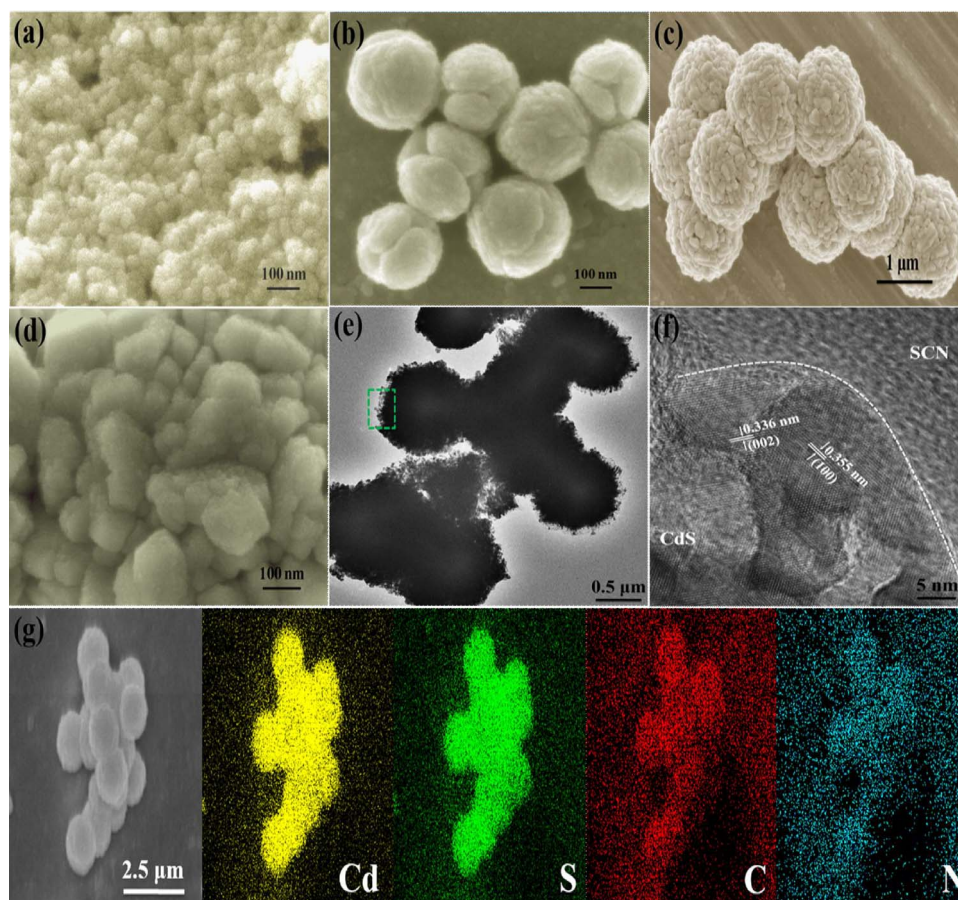
Fig. 3. SEM images of the exfoliated SCN (a), CdS (b) and CS5 composite (c, d); TEM (e) and HRTEM (f) images of the CS5 composite, together with the EDS elemental mapping analysis of CS5 composite (g). (For interpretation of the references to colour in text, the reader is referred to the web version of this article).

petal sub-units. Fig. 3(c) and (d) show the images of the CS5 composite, which indicate that, after mixing with exfoliated SCN in solution, the surface of the CdS microspheres is coated with exfoliated SCN sized around an average of 1 μm. The contoured structure of the CdS enables the exfoliated SCN to easily anchor and adhere to the surface. The TEM image in Fig. 3(e) affirms that the surface of the CdS is covered by the exfoliated SCN. Furthermore, the HRTEM image in Fig. 3(f) shows clearly that the lattice fringes of 0.355 nm and 0.336 nm are attributed to respectively the (100) and (002) planes of CdS. Additionally, the clear interface between CdS and SCN was formed during the SCN coating process, which is very important for efficient charge transfer between CdS and SCN. To further clarify the composition profile of the CS5 composite, SEM-mapping analysis was applied. As shown in Fig. 3(g), Cd (yellow) and S (green) elements were distributed uniformly on the CdS nanoparticles, and the even dispersion of C (red) and N (blue) elements is indicative of the uniform distribution of SCN on the CdS surface.

3.2. Chemical states

XPS analysis was performed for exfoliated SCN and CS5 composite to examine the chemical composition of the as-prepared samples and elucidate the corresponding chemical states of the elements. Fig. 4 presents the typical XPS spectra of the exfoliated SCN and CS5 composite. The survey spectrum (Fig. 4(a)) of the exfoliated SCN sample revealed three photoelectron peaks at binding energies 532.0 eV (O 1s), 399.0 eV (N 1s), 288.0 eV (C 1s), and 168.0 eV (S 2p), and no obvious peak corresponding to sulfur was present because the content of sulfur was very low in the sample. In Fig. 4(b), the S 2p peak was split into two peaks centered at 164.0 and 168.2 eV, with the weaker peak 164.0 eV

corresponding to C−S bonds formed by substituting sulfur with lattice nitrogen, and the stronger peak at 168.2 eV indicating the presence of SO_4^{2-} [33,34]. Fig. 4(c) shows that the C 1s spectrum of SCN can be deconvoluted into three peaks at 284.6 eV, 286.1 eV and 288.1 eV. The peak at 284.6 eV is typically ascribed to sp^2 C−C bonds, and the peak at 288.1 eV is identified as sp^2-bonded carbon in N-containing aromatic rings (N−C=N), which represent the major carbon species in the exfoliated SCN [35,36]. The weak peak at 286.2 eV could be assigned to sp^3-coordinated carbon bonds from the defects on the exfoliated SCN surfaces [37]. As shown in Fig. 4(d), the N 1s spectral envelope of exfoliated SCN contains peaks at 398.8, 399.9, and 401.0 eV that are indicative of C−N=C, N−$(C)_3$ and amine functionalities, respectively [38], while the peak at 405.7 eV corresponds to highly oxidized chain terminations in the polymer matrix [39]. The XPS survey in Fig. 4(a) indicates that the oxygen content of exfoliated SCN is higher than that of pure graphic carbon nitride. After the addition of CdS, three peaks centered at 398.8, 399.1 and 403.9 eV can be identified (Fig. 4(d)). The main peak centered at 398.8 eV originates from the sp^2-bonded N involved in the triazine rings (C−N=C), confirming the presence of sp^2-bonded exfoliated SCN. Compared with pure SCN, the lower binding energy at 403.9 eV and the peak disappearance at 401.0 eV demonstrate the strong electric coupling interaction between SCN and CdS, suggesting the heterojunction formation at the amine functionalities site and the oxidized chain terminations. Moreover, the photoelectron peaks for Cd 5d (Fig. 4(e)) appeared at 404.9 and 411.7 eV, which are assigned respectively to the Cd $5d_{5/2}$ and Cd $5d_{3/2}$ for Cd^{2+} in the CdS nanostructure [40]. The S 2p peaks at 161.2 eV (S $2p_{3/2}$) and 162.4 eV (S $2p_{1/2}$) (Fig. 4(f)) are ascribed to be S^{2-} in the CdS nanostructure [41]. Thus, from the XPS results, it can be inferred that the CdS has been successfully hybridized with the exfoliated SCN via the formation
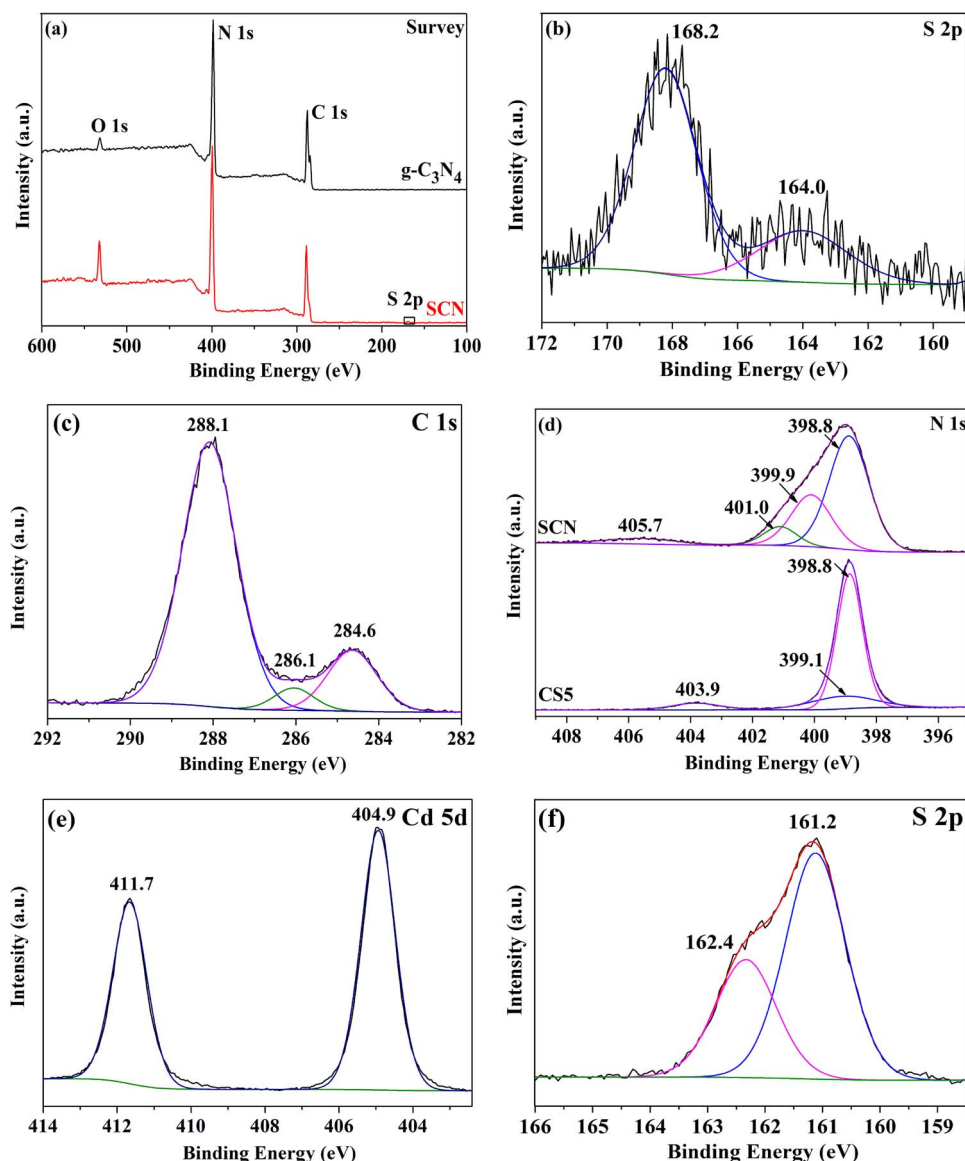
Fig. 4. XPS survey (a) spectra of g-C$_3$N$_4$ and exfoliated SCN; high-resolution XPS spectra of S 2p region (b), C 1s region (c) and N 1s region (d) of the exfoliated SCN; high-resolution XPS spectra of N 1s region (d), Cd 5d region (e) and S 2p (f) of the CS5 composite.

of heterojunction, which provides for the photo-induced charge transfer between two semiconductors.

3.3. Optical property

The optical absorption properties of CdS, exfoliated SCN and the CS composites were investigated by UV–vis diffuse reflectance spectroscopy (DRS), as shown in Fig. 5(a). The exfoliated SCN exhibited an absorption edge at approximately 450 nm, corresponding to 2.76 eV of bandgap energy based on the correlation $E_g = 1240/\lambda$ [42], while the pure CdS showed a visible light absorption edge at approximately 540 nm, corresponding to 2.29 eV of bandgap energy. In particular, the CS5 composite displayed higher absorption intensities in the visible light region than exfoliated SCN and CdS, signifying that the composites are promising visible-light photocatalysts. Typically, the energy bandgap values of CdS, exfoliated SCN and CS composites can be estimated using the Kubelka–Munk function:

$$\alpha h \nu = A (h \nu - E_g)^{n/}$$

where α, h, ν, h, E_g, and A are the absorption coefficient, Planck constant, light frequency, band gap energy, and a constant, respectively.

The coefficient n relies on the type of optical transition of the semiconductor (n = 1 for direct transition and n = 4 for indirect transition), and is 1 for CdS [43] and 4 for SCN [44]. In the plot of $(\alpha h\nu)^{0.5}$ vs (hv) (Fig. 5(b)), the band gaps of exfoliated SCN, CdS, CS2, CS5, CS8 and CS10 composite were calculated to be 2.76, 2.29, 2.32, 2.29, 2.36 and 2.38 eV, respectively.

It is well-known that the photoluminescence (PL) emission is important to disclose the fate of the electron-hole pairs in the semiconductor because PL emission results from the recombination of photo-generated electrons and holes for the semiconductors [45]. The higher intensity of the PL spectra is, the faster recombination of the electrons and holes is, and thereby the lower the photocatalytic activity is. Fig. 6(a) presents the PL spectra of CdS and the CS composites at an excitation wavelength of 325 nm. The pure CdS and all the CS composite exhibited the similar peaks at the wavelength of around 647 nm in the PL spectra. On one hand, the peak intensities of CS2 and CS5 were weaker than that of the pure CdS, suggesting that the recombination rates of the photo-generated electrons and holes were relatively retarded. On the other hand, as the composition of exfoliated SCN increased, the peak intensities of CS8 and CS10 were greater than CdS, which indicates elevated rates. Notably, the CS5 composite had
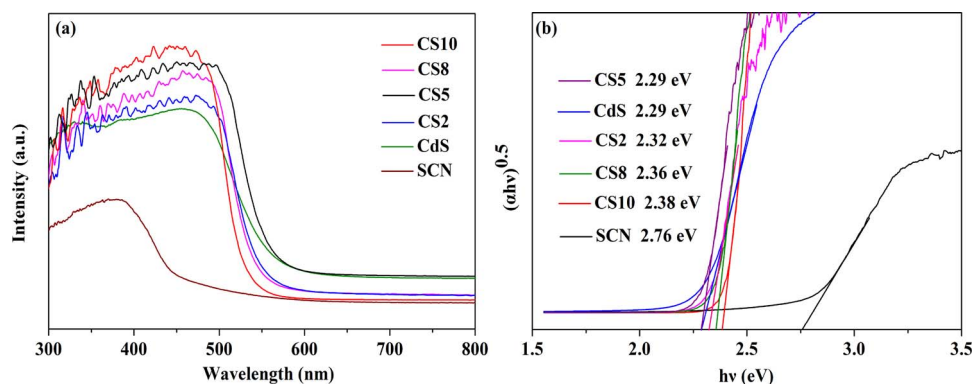
Fig. 5. (a) UV–vis diffuse reflectance spectra and (b) plot of $(\alpha h\nu)^{0.5}$ vs. $h\nu$ (photon energy) of the exfoliated SCN, CdS, CS2, CS5, CS8 and CS10 composite.

the lowest peak magnitude, which indicates the lowest photo-generated electron–hole $(e^- – h^+)$ recombination rate, and thereby implies that the greatest photocatalytic activity.

The time-resolved fluorescence decay spectra provide important information about the exciton lifetime which represents a crucial indicator of the efficiency of the radiative recombination of the photo-induced charges. The results of the measurements are shown in Fig. 6(b) and summarized in Table 1. Fig. 6(b) shows that both the pure CdS and CS5 composite exhibited biexponential decay, and the fluorescence peak decay of the CS5 composite was slower than that of CdS. The biexponential decay of the CS5 composite suggested that two emissive states were involved in the PL decay with half-lives of $\tau 1 = 2.7525\,\mu s$ and $\tau 2 = 13.1317\,\mu s$. The fast decay constant $(\tau 1)$ can be attributed to the radiative emission of the direct inter-band exciton recombination, while the much slower decay constant $(\tau 2)$ to the radiative emission via indirect recombination of trapped electrons with valence band (VB) holes [46–48]. As shown in Table 1, the $\tau 1$ and $\tau 2$ values for CS5 were longer than that for CdS, suggesting that the lifetime of photo-generated charge carriers was prolonged and a more effective separation of electrons and holes in CS5 composite. A longer fluorescence lifetime of carriers improves photocatalytic activity. Hence, the results of the extended lifetime of the photo-induced carriers of the CS5 composite further illustrate that the introduction of the exfoliated SCN can efficiently retard the recombination of the carriers and thereby enhance the likelihood of the charge carriers participating in photocatalytic degradation.

3.4. Photoelectrochemical response

The photocurrents of the exfoliated SCN, CdS and CS5 composite were assessed to further understand the photoelectric performance in terms of the separation efficiency of photo-generated electron-hole pairs [49]. The higher the photocurrent density is, the more efficient charge separation and transportation are. Fig. 7 shows the transient

Table 1
Parameters of the time-resolved PL decay curves.

Sample	B_1 (%)	τ_1 (μs)	B_2 (%)	τ_2 (μs)
CdS	9.09	2.3864	90.91	12.5064
CS5	14.76	2.7525	85.24	13.1317

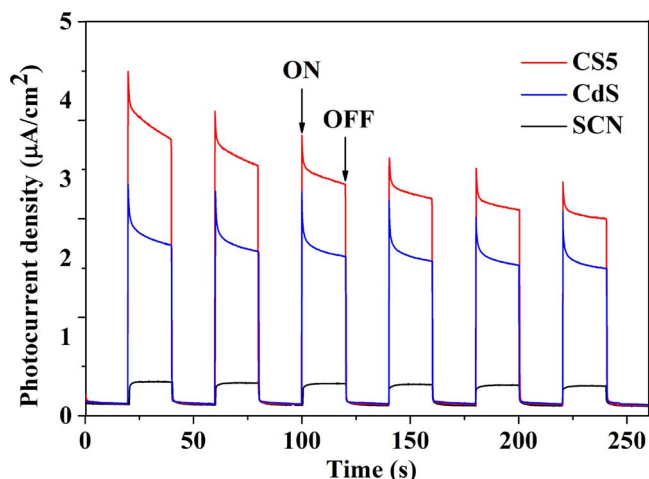Fitted equation: $R(t) = B_1 e^{(-t/\tau 1)} + B_2 e^{(-t/\tau 2)}$.

Fig. 7. Photocurrent (PC) response analysis of the exfoliated SCN, CdS and CS5 composite under intermittent visible light irradiation.

photocurrent density versus irradiation time recorded under visible light irradiation. The photocurrent density increased sharply when the light was switched on, and immediately returned to its initial negligible value after the light source was turned off, and the peak values decreased slightly as the cycles repeated which indicates that the as-
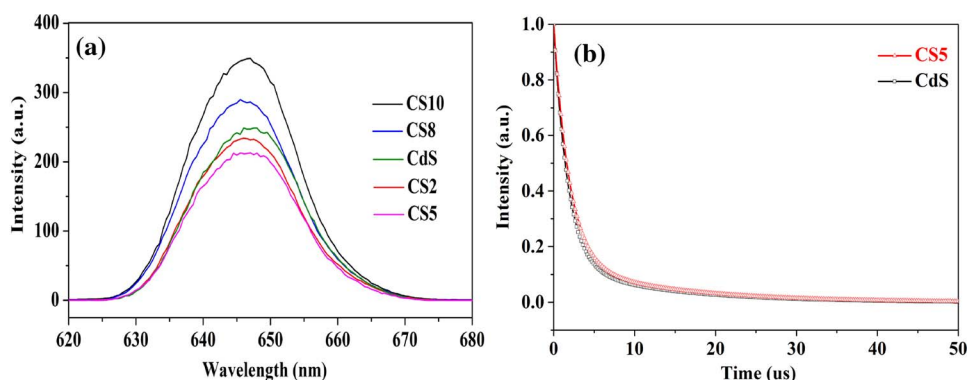

Fig. 6. Photoluminescence spectra (a) and time-resolved fluorescence decay spectra (b) of as-synthesized photocatalysts at an excitation wavelength of 325 nm.
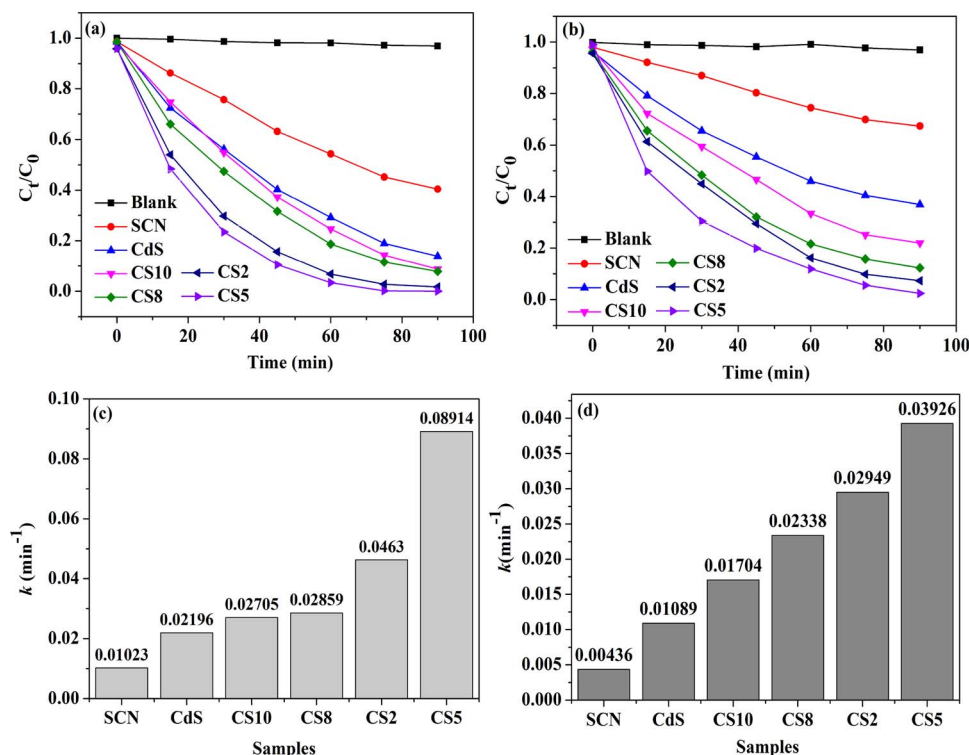
Fig. 8. Photocatalytic RhB (a) and BPA (b) degradation performance with respect to time; degradation rate constants of RhB (c) and BPA (d) based on pseudo-first order kinetics.
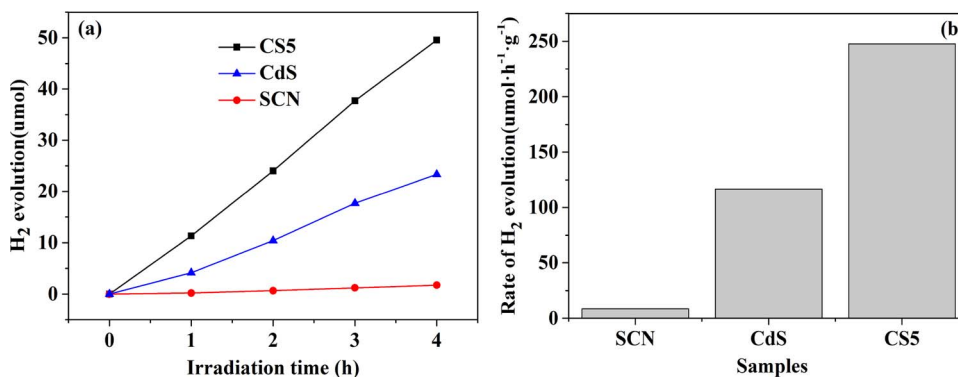

Fig. 9. Visible-light photocatalytic H_2 evolution of exfoliated SCN, CdS and CS5 composite: (a) cumulative amount of H_2 with time; and (b) H_2 evolution rate.

prepared samples exhibited excellent structural stabilities. Comparatively, the transient photocurrent density during irradiation was the greatest for CS5, followed by CdS then the exfoliated SCN. The highest photocurrent response of the CS5 composite is tied to the suppressed recombination probability of the photogenerated electrons and holes via the transfer of CS5 heterojunction structures, which is consistent with our above discussions and photocatalytic activity measurements.

3.5. Photocatalytic activity

3.5.1. Photocatalytic degradation of RhB and BPA

The photocatalytic activities of as-prepared samples were determined by the degradation of RhB and BPA under visible light illumination, and results are shown in Fig. 8. Each of the photodegradation reactions was performed after 60 min of adsorption equilibrium in the absence of visible light, and the "blank" curves in Fig. 8(a) and (b) represent the absence of any photocatalyst, which indicates negligible degradation of the dyes. In the presence of photocatalysts, the concentrations of both RhB and BPA decreased fastest for the CS composites, followed by pure CdS then the exfoliated SCN (Fig. 8(a) and (b)).

Among the CS composites, CS5 exhibited the most efficient degradation, followed by CS2, CS8 then CS10, as also quantified by the rate constants in Fig. 8(c) and (d). In general, the degradation kinetics were faster for RhB (Fig. 8(c)) than BPA (Fig. 8(d)), and the rate constants of CS5 were almost an order-of-magnitude greater than that of the exfoliated SCN and 1.3 – 3.3 times that of other composites for both RhB and BPA. The above results reveal that the hybridization of exfoliated SCN on the CdS particles remarkably improved the photocatalytic efficiency, but an optimal amount of SCN existed. On one hand, the exfoliated SCN can enhance the adsorption capacity for pollutants, which can enrich the pollutant molecules on the surface of the photoactive CdS particles, and thus resulting in the acceleration of the photocatalytic reactions. On the other hand, a thick and dense layer of exfoliated SCN may reduce the inherent optical absorption of CdS and result in a rapid decrease in photogenerated charges, and ultimately reducing the photocatalytic activity [50,51].

3.5.2. Photocatalytic hydrogen (H_2) generation

To evaluate the photocatalytic performance of the as-prepared photocatalysts, hydrogen evolution experiments from water splitting
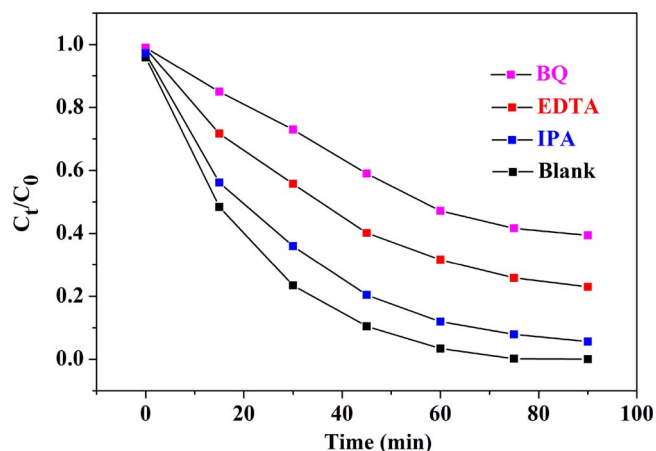
Fig. 10. Effects of different reactive species scavengers on the photo-degradation of RhB by the CS5 composite under visible-light irradiation.

were carried out under visible light irradiation. Fig. 9(a) shows that the cumulative H_2 increased with time, with that for CS5 increasing the fastest, followed by CdS then CS5. This indicates that the CS5 composite exhibited improved photocatalytic hydrogen generation activity as compared to the pure constituents. Fig. 9(b) further quantifies the average H_2 production rates of the as-obtained samples as 8, 117 and 248 $\mu mol\, h^{-1}\, g^{-1}$ for the exfoliated SCN, CdS and CS5, respectively. These results indicate that the hydrogen production rates of CS5 are significantly enhanced by coupling the exfoliated SCN nanosheets with CdS, because of the heterojunction electric field generated.

3.6. Photocatalytic mechanism

As is well-acknowledged, the super oxide radical ($\cdot O_2^-$), hydroxyl radical ($\cdot OH$) and hole (h^+) are the major reactive species for a photocatalytic oxidation reaction [52]. In order to investigate the free radicals in the reaction process of selective oxidation of aromatic alcohols to aromatic aldehydes, a series of experiments were carried out. In this study, p-benzoquinone (BQ), isopropyl alcohol (IPA) and disodium ethylenediaminetetraacetate (EDTA-2Na) were adopted as the scavengers of $\cdot O_2^-$, $\cdot OH$ and h^+, respectively. Fig. 10 shows the degradation of RhB by the CS5 composite with time in the absence of any quencher and the presence of each of the three quenchers. As depicted in Fig. 10, it is clear that the photocatalytic performance decrease after adding the EDTA-2Na or BQ, which implies the $\cdot O_2^-$ and h^+ were the dominant species in the degradation of RhB. However, in the presence of IPA, the photodegradation rate of RhB exhibited lesser decrease, revealing that the $\cdot OH$ active species were less dominant in the photocatalytic reaction. Based on the above results, it could be deduced that the $\cdot O_2^-$, $\cdot OH$ and h^+ played an important role in the photodegradation process by the CS5 composite.

To further identify the radical generation in the photo-catalytic system under visible light irradiation, the ESR spin-trap experiments were performed on pure CdS and the CS5 composite. All the experiments were operated either in darkness or visible light irradiation durations of 5 min or 10 min. As indicated in Fig. 11(a) and (b), there was no signal in the dark, and the peak intensities increased with irradiation duration. Specifically, when the light was on for both CdS (Fig. 11(a)) and the CS5 composite (Fig. 11(b)), four characteristic peaks and four corresponding troughs of DMPO-$\cdot O_2^-$ were obtained, indicating that $\cdot O_2^-$ was produced during the photodegradation process. Comparing Fig. 11(a) and (b), the CS5 composite had greater peak values than CdS, suggesting that the amount of $\cdot O_2^-$ radicals produced in the CS5 heterojunction photocatalyst surface were more than those of pure CdS, and that $\cdot O_2^-$ was a major active species participating in the photocatalytic degradation reaction. Furthermore, the intensities of the

peaks of the spin-trapped TEMPO-h^+ increased when exposed to visible light irradiation relative to that in the dark for both the pure CdS (Fig. 11(c)) and CS5 composite (Fig. 11(d)). The characteristic signals at g-values (i.e., the spectral splitting factor) of 1.9992 and 1.9995 were also detected for the pure CdS and CS5 composite, respectively, providing evidence of sulfur vacancies located at the surface [53,54]. As shown in Fig. 11(e) and (f), the intensities of the DMPO-$\cdot OH$ adducts were negligible in the dark but the absolute peak and trough values became greater with longer durations of visible light irradiation, demonstrating that $\cdot OH$ played an important role in the photocatalytic process. Similar to that for DMPO-$\cdot O_2^-$ (Fig. 11(a) and (b)), the peak values of the CS5 composite (Fig. 11(e)) were higher than those for pure CdS (Fig. 11(f)), which indicates that the amount of $\cdot OH$ radicals generated was higher for the former. Hence, the radicals trap experiments and ESR analysis reveal that the photocatalytic process was governed by the combined effect of $\cdot O_2^-$, h^+ and $\cdot OH$. The synergetic effect resulting from hybridizing exfoliated SCN and CdS favor the separation of charge carriers, leading to enhanced active species generation and thereby improvement of the photocatalytic degradation of RhB and BPA.

The photocatalytic degradation mechanism by the CS5 composite via the transfer of charge carrier and the formation of oxidizing radical species is schematically proposed in Fig. 12. With regards to the charge carrier transfer of the CS5 composite, it is hypothesized that the photogenerated electrons in the conducting band (CB) of the exfoliated SCN migrates to the CB of CdS, and the holes in the valence band (VB) of CdS migrate to the VB of the exfoliated SCN due to the potential difference. After the transfer of the photogenerated electrons from the CB of exfoliated SCN to the CB of CdS, the accumulated electrons with a more negative potential of $-0.52\, eV$ can oxidize the dissolved oxygen adsorbed onto the surface of CdS to yield $\cdot O_2^-$ ($E_{O_2/\cdot O_2^-} = -0.33\, eV$) and subsequently produce $\cdot OH$. The resulting reactive species (namely, $\cdot OH$ and $\cdot O_2^-$) can efficiently degrade the pollutants. Meanwhile, the strongly oxidized holes, transferred to the VB of SCN, can not only effectively prevent the photocorrosion of CdS, but also directly degrade the RhB and BPA molecules on the surface of exfoliated SCN. The oxidizing species have been clearly confirmed by the ESR signals and trapping experiments (Figs. 10 and 11).

3.7. Recyclability and stability

Other than photocatalytic efficiency, stability for recovery and reuse is also an important factor to measure the quality of the catalysts because of the photocorrosion or photodissolution that may occur on the photocatalyst surface during the photocatalytic process. Accordingly, the stability of the best-performing CS5 composite was investigated by repeatedly photodegrading RhB over four cycles under the same conditions. Specifically, after every 90 min of photodegradation (i.e., one cycle), the photocatalysts were centrifuged, washed with ethanol and distilled water, and then dried. Fig. 13(a) shows only a slight drop in the efficiency of RhB degradation results by the CS5 composite with every cycle, the drop of which was at least in part due to the loss of photocatalysts during the centrifugation and washing steps. Therefore, the results indicate that the CS5 composite was relatively photo-stable throughout the photocatalytic process. In addition, the XRD spectra of the CS5 composite before and after the four cycles of degradation was also obtained, as shown in Fig. 13(b). No significant difference in the diffraction peak positions are observed, demonstrating a very stable crystal structure even after the repeated degradations. Fig. 13 hence affirms that the stability of the CS5 composite for repeated use as an efficient visible-light photocatalyst for wastewater treatment applications.

4. Conclusions

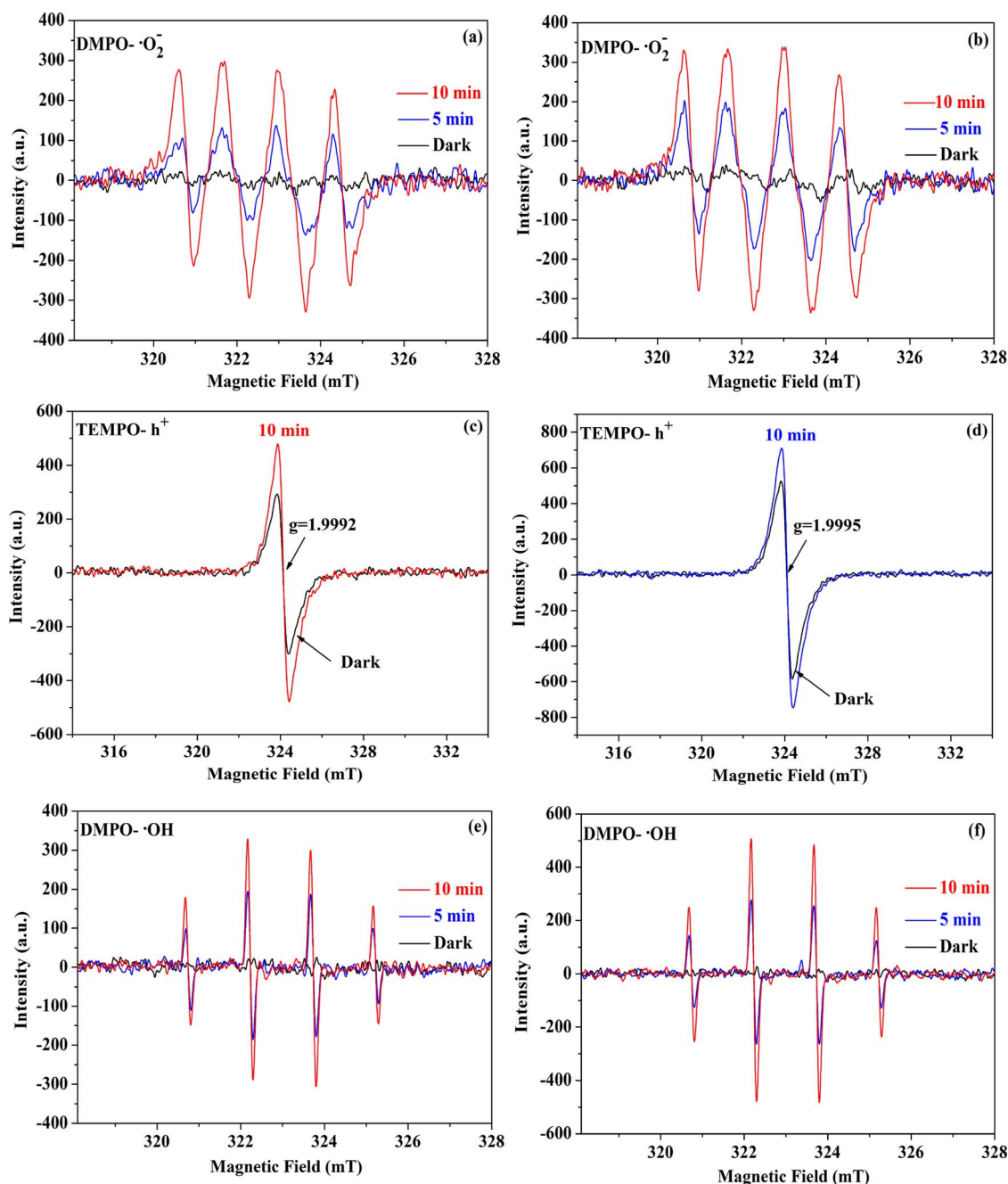In summary, we have developed a facile one-pot solvothermal

Fig. 11. ESR spectra of radical adducts trapped by DMPO ($\cdot O_2^-$ and $\cdot OH$) and TEMPO (h^+) either in the dark or under visible light irradiation durations of 5 or 10 min: in methanol dispersion for DMPO- $\cdot O_2^-$ of CdS (a) and CS5 (b); in aqueous dispersion for TEMPO-h^+ of CdS (c) and CS5 (d); and in aqueous dispersion for DMPO- $\cdot OH$ $^-$ of CdS (e) and CS5 (f).

method to synthesize exfoliated sulfur-doped carbon nitride-coated CdS nanostructures with uniform morphology. Results indicate that a strong electric coupling interaction existed between SCN and CdS due to the heterojunction formed at the amine functionalities sites and oxidized chain terminations of SCN. The resulting hybrid composite possessed not only superior performance of visible light absorption, but also improved the separation efficiency and prolonged the lifetime of charge carriers. Specifically, the best-performing as-synthesized CdS/SCN composite (i.e., namely, the CS5) exhibited (i) enhanced visible-light-driven photocatalytic RhB degradation efficiency that was about 8.71 and 4.06 times higher than those of exfoliated SCN and CdS, respectively; (ii) enhanced visible-light-driven photocatalytic BPA degradation efficiency that was 9.00 and 3.61 times higher than those of exfoliated SCN and CdS, respectively; and (iii) more efficient visible-light photocatalytic H_2 generation rate ($247.72 \, \mu mol \, h^{-1} \, g^{-1}$) than the

constituents. The exfoliated sulfur-doped carbon nitride nanocoating not only protected the CdS surface from photodegradation and enhanced visible light absorption, but also facilitated the separation of the photogenerated charges. Cycling experiments indicated the excellent photostability and thereby the composites synthesized are promising for long-term photocatalytic applications. It is believed that this synthesis method can be extended to prepare a wide variety of functional nanohybrids for wide-ranging applications.
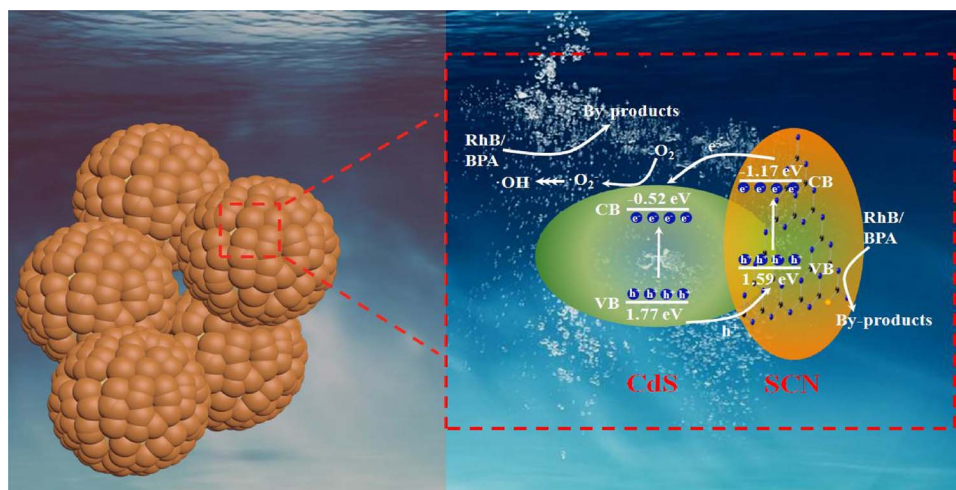
Acknowledgments

Fig. 12. The mechanism of electrons/holes transfer and separation process of the CS5 composite under visible light irradiation.
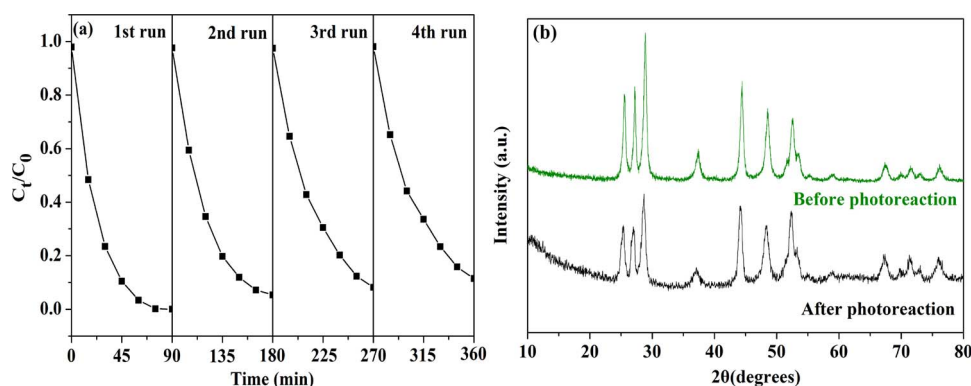

Fig. 13. (a) Photocatalytic degradation of RhB by the CS5 composite under visible-light irradiation over 4 cycles; (b) XRD patterns of the CS5 composite before and after 4 cycles of photocatalytic RhB degradation.

References

[1] H. Wang, X.Z. Yuan, Y. Wu, G.M. Zeng, H.R. Dong, X.H. Chen, L.J. Leng, Z.B. Wu, L.J. Peng, Appl. Catal. B Environ. 186 (2016) 19–29.

[2] L. Xu, C. Srinivasakannan, J.H. Peng, L.B. Zhang, D. Zhang, J. Alloy Compd. 695 (2017) 263–269.

[3] H. Wang, X.Z. Yuan, Y. Wu, G.M. Zeng, X.H. Chen, L.J. Leng, Z.B. Wu, L.B. Jiang, H. Li, J. Hazard. Mater. 286 (2015) 187–194.

[4] X. Wang, K. Maeda, A. Thomas, K. Takanabe, G. Xin, J.M. Carlsson, K. Domen, M. Antonietti, Nat. Mater. 8 (2009) 76–80.

[5] W.J. Ong, L.L. Tan, Y.H. Ng, S.T. Yong, S.P. Chai, Chem. Rev. 116 (2016) 7159–7329.

[6] Z. Zhao, Y. Sun, F. Dong, Nanoscale 7 (2015) 15–37.

[7] S.M. Lam, J.C. Sin, A.R. Mohamed, Mater. Sci. Semicond. Process. 47 (2016) 62–84.

[8] S.C. Yan, Z.S. Li, Z.G. Zou, Langmuir 26 (2010) 3894–3901.

[9] X. Bai, R. Zong, C. Li, D. Liu, Y. Liu, Y. Zhu, Appl. Catal. B Environ. 147 (2014) 82–91.

[10] Y.J. Zhang, T. Mori, J.H. Ye, M. Antonietti, J. Am. Chem. Soc. 132 (2010) 6294.

[11] G.D. Ding, W.T. Wang, T. Jiang, B.X. Han, H.L. Fan, G.Y. Yang, ChemCatChem 5 (2013) 192–200.

[12] T.T. Li, L.H. Zhao, Y.M. He, J. Cai, M.F. Luo, J.J. Lin, Appl. Catal. B Environ. 129 (2013) 255–263.

[13] J.X. Sun, Y.P. Yuan, L.G. Qiu, X. Jiang, A.J. Xie, Y.H. Shen, J.F. Zhu, Dalton Trans. 41 (2012) 6756–6763.

[14] G. Liu, P. Niu, C.H. Sun, S.C. Smith, Z.G. Chen, G.Q. Lu, H.M. Cheng, J. Am. Chem. Soc. 132 (2010) 11642–11648.

[15] Y. Zhang, M. Park, H.-Y. Kim, S.J. Park, J. Alloys Compd. 686 (2016) 106–114.

[16] Y. Zhang, M. Park, H.Y. Kim, B. Ding, S.J. Park, Appl. Surf. Sci. 384 (2016) 192–199.

[17] X.L. Li, Y. Jia, A.Y. Cao, ACS Nano 4 (2012) 506–512.

[18] Z.X. Pan, H. Zhang, K. Cheng, Y.M. Hou, J.L. Hua, X.H. Zhong, ACS Nano 6 (2012) 3982–3991.

[19] A. Ferancová, S. Rengaraj, Y. Kim, J. Labuda, M. Sillanpää, Biosens. Bioelectron. 26 (2010) 314–320.

[20] Y. Hu, Y. Liu, H.S. Qian, Z.Q. Li, J.F. Chen, Langmuir 26 (2010) 18570–18575.

[21] Y. Liu, L. Zhou, Y. Hu, C.F. Guo, H.S. Qian, F.M. Zhang, X.W. Lou, J. Mater. Chem. 21 (2011) 18359–18364.

[22] W.L. Yang, Y. Liu, Y. Hu, M.J. Zhou, H.S. Qian, J. Mater. Chem. 22 (2012) 13895–13898.

[23] X.B. Chen, S.H. Shen, L.J. Guo, S.S. Mao, Chem. Rev. 110 (2010) 6503–6570.

[24] D.N. Ke, S.L. Liu, K. Dai, J.P. Zhou, L.N. Zhang, T.Y. Peng, J. Phys. Chem. C 113 (2009) 16021–16026.

[25] A. Kudo, Y. Miseki, Chem. Soc. Rev. 38 (2009) 253–278.

[26] Y. Guo, H.S. Wang, C.L. He, L.J. Qiu, X.B. Cao, Langmuir 25 (2009) 4678–4684.

[27] P.X. Qiu, C.M. Xu, H. Chen, F. Jiang, X. Wang, R.F. Lu, X.R. Zhang, Appl. Catal. B Environ. 206 (2017) 319–327.

[28] B. Lin, H. An, X.Q. Yan, T.X. Zhang, J.J. Wei, G.D. Yang, Appl. Catal. B Environ. 210 (2017) 173–183.

[29] H.X. Zhao, H.T. Yu, X. Quan, S. Chen, Y.B. Zhang, H.M. Zhao, H. Wang, Appl. Catal. B Environ. 152–153 (2014) 46–54.

[30] Y. Sui, J.H. Liu, Y.W. Zhang, X.K. Tian, W. Chen, Nanoscale 5 (2013) 9150–9155.

[31] J.G. Yu, K. Wang, W. Xiao, B. Cheng, Phys. Chem. Chem. Phys. 16 (2014) 11492–11501.

[32] S. Tonda, S. Kumar, Y. Gawli, M. Bhardwaj, S. Ogale, Int. J. Hydrogen Energy 2 (2017) 5917–5984.

[33] G. Liu, P. Niu, C.H. Sun, S.C. Smith, Z.G. Chen, G.Q. Lu, H.M. Cheng, J. Am. Chem. Soc. 132 (2010) 11642–11648.

[34] J.D. Hong, X.Y. Xia, Y.S. Wang, R. Xu, J. Mater. Chem. 22 (2012) 15006–15012.

[35] Y. Wang, X. Wang, M. Antonietti, Angew. Chem. Int. Ed. 51 (2012) 68–89.

[36] A. Vinu, Adv. Funct. Mater. 18 (2008) 816–827.

[37] G. Zhang, J. Zhang, M. Zhang, X. Wang, J. Mater. Chem. 22 (2012) 8083–8091.

[38] Q. Xiang, J. Yu, M. Jaroniec, J. Phys. Chem. C 115 (2011) 7355–7363.

[39] K.L. Corp, C.W. Schlenker, J. Am. Chem. Soc. 139 (2017) 7904–7912.

[40] J. Chu, X. Li, J. Qi, Crystengcomm 14 (2012) 1881–1884.

[41] V.L. Colvin, A.N. Goldstein, A.P. Alivisatos, J. Am. Chem. Soc. 114 (1992) 5221–5230.

[42] J. Long, S. Wang, Z. Ding, S. Wang, Y. Zhou, L. Huang, X. Wang, Chem.Commun. (Camb.) 48 (2012) 11656–11658.

[43] K. Li, M. Han, R. Chen, S. Li, S. Xie, C. Mao, X. Bu, X. Cao, L. Dong, P. Feng, Y. Lan, Adv. Mater. 28 (2016) 8906–8911.

[44] C. Li, Y. Du, D. Wang, S. Yin, W. Tu, Z. Chen, M. Kraft, G. Chen, R. Xu, Adv. Funct. Mater. 27 (2014) 1604328–1604335.

[45] L.H. Lin, H.H. Ou, Y.F. Zhang, X.C. Wang, ACS Catal. 6 (2016) 3921–3931.

[46] N.S. Han, H.S. Shim, J.H. Seo, S.Y. Kim, S.M. Park, J.K. Song, J. Appl. Phys. 107 (2010) 084306.

[47] M.V. Dozzi, C.D. Andrea, B. Ohtani, G. Valentini, E. Selli, J. Phys. Chem. C 117 (2013) 25586–25595.

[48] Y. Yu, P. Zhang, L. Guo, Z. Chen, Q. Wu, Y. Ding, W. Zheng, Y. Cao, J. Phys. Chem.C 118 (2014) 12727–12733.

[49] W.T. Wu, J.Q. Zhang, W.Y. Fan, Z.T. Li, L.Z. Wang, X.M. Li, Y. Wang, R.Q. Wang, J.T. Zheng, M.B. Wu, H.B. Zeng, ACS Catal. 6 (2016) 3365–3371.

[50] Y.Y. Li, J.P. Liu, X.T. Huang, J.G. Yu, Dalton Trans. 39 (2010) 3420–3425.

[51] Y. Hu, X.H. Gao, L. Yu, Y.R. Wang, J.Q. Ning, S.J. Xu, X.W. Lou, Angew. Chem. Int. Ed. 52 (2013) 5636–5639.

[52] H. Wang, X.Z. Yuan, Y. Wu, G.M. Zeng, W.G. Tu, C. Sheng, Y.C. Deng, F. Chen, J.W. Chew, Appl. Catal. B Environ. 209 (2017) 543–553.

[53] Y. Yin, J.C. Han, Y.M. Zhang, X.H. Zhang, P. Xu, Q. Yuan, L. Samad, et al., J. Am. Chem. Soc. 138 (2016) 7965–7972.

[54] S.Z. Hu, Y.M. Li, F.Y. Li, Z.P. Fan, H.F. Ma, W. Li, X.X. Kang, ACS Sustain. Chem. Eng. 4 (2016) 2269–2278.